Nano Research

Open Access

Research Article

Two-dimensional lateral magnetic tunnel junction with ultrahigh tunneling magnetoresistance

Qiu-Qiu Li[1], Zhi-Fu Duan[1], Wen-Wen Liu[2], Rong Yang[1] ✉, Bo Li[1,3,4] ✉, and Ke-Qiu Chen[2] ✉

[1] *Changsha Semiconductor Technology and Application Innovation Research Institute, College of Semiconductors (College of Integrated Circuits), Hunan University, Changsha 410082, China*
[2] *Department of Applied Physics, School of Physics and Electronics, Hunan University, Changsha 410082, China*
[3] *Research Institute of Hunan University in Chongqing, Chongqing 401120, China*
[4] *Shenzhen Research Institute of Hunan University, Shenzhen 518063, China*

Cite this article: *Nano Research*, **2025**, *18*, 94907188. https://doi.org/10.26599/NR.2025.94907188

ABSTRACT: Giant tunneling magnetoresistance (TMR) has always been a pursuit in the research of magnetic tunnel junctions (MTJ). Two-dimensional (2D) magnetic materials have been used to construct lateral MTJ with high TMR. Here we investigated the crystal structure and magnetic property of CrSI monolayer, and found that it is a ferromagnetic semiconductor with a Curie temperature of about 180 K. The CrSI monolayer with Li adsorption (Li-CrSI) show ferromagnetic half-metallic with a high Curie temperature of 300 K. Further we designed a lateral Li-CrSI/CrSI/Li-CrSI monolayer MTJ. The TMR of the MTJs along *b* transport direction is 3 orders of magnitude times larger than that of the *a* transport direction, which should result from the different spin filtering ability along the two directions. The TMR of *b* transport direction in the MTJ is 7.67 × 10^{14}, which is significantly higher than that of any reported lateral MTJs based on 2D materials. Our results provide a promising avenue for designing lateral MTJs with giant TMR and high Curie temperature.

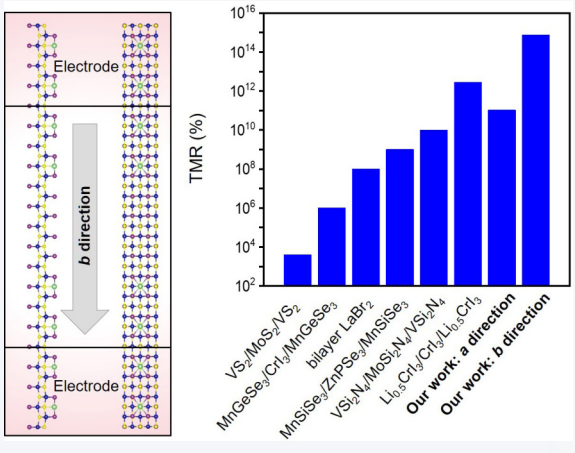

KEYWORDS: two-dimensional materials, magnetic tunnel junctions, CrSI monolayer, tunneling magnetoresistance, Li atom adsorption

1 Introduction

Magnetic tunnel junction (MTJ) which is generally composed of metal electrodes and semiconductor tunnel barrier plays an important role in the spintronic devices [1–4]. The focus of the MTJs research is to achieve giant tunneling magnetoresistance (TMR). In the past two decades, conventional ferromagnetism like Co_2MnSi and CoFeB are used as electrodes and MgO is used as tunnel barrier to obtain a giant TMR [5, 6]. While in the construction of conventional MTJs, the lattice matching between different thin films is one issue that must be considered, which greatly limits the exploration of giant TMR. Thus it is urgent to investigate novel magnetic materials and MTJs with novel structure to achieve giant TMR.

In recent years, two-dimensional (2D) van der Waals (vdW) layered materials with atomic thickness and dangling bond free surface are sensitive to external control and have the great potential applications in electronic, optoelectronic and spintronic application [7–10]. The vdW heterostructures composed by 2D materials can break through the limitations of lattice matching and have high-quality contact interface, showing excellent electrical and magnetoelectronic properties [11–15]. For example, the multiple-spin-filter MTJ based on graphene/CrI_3 heterostructure show a record TMR of 19,000% at 2 K [16]. The antiferromagnetic MTJ formed by twisting two bilayers of CrSBr show a nonvolatile TMR of more than 700% at 2 K [17]. In theoretical investigation, vertical and lateral MTJ composed by 2D materials have been extensively studied and show excellent TMR. Li atom adsorption and intercalation can alter or tuning the electronic properties of 2D magnetic materials [18], such as transforming semiconductor materials into half-metallic state [19–21], increasing the Curie

Received: November 25, 2024; **Revised:** December 8, 2024
Accepted: December 12, 2024

✉Address correspondence to Rong Yang, yangrong@hnu.edu.cn; Bo Li, boli@hnu.edu.cn; Ke-Qiu Chen, keqiuchen@hnu.edu.cn

temperature of magnetic materials [22, 23]. The TMR of vertical and lateral $Li_{0.5}CrI_3/CrI_3/Li_{0.5}CrI_3$ MTJ are 1.48×10^{14} and 2.86×10^{12}, respectively, showing huge potential of 2D materials in the application of MTJ [21].

vdW layered CrSX (X = Cl, Br, I) with orthorhombic structure exhibits an in-plane easy axis and its magnetism in the plane is also anisotropic [24, 25]. CrSX has attracted huge attention in the strain modulation, magnetic anisotropy and magneto-transport measurement [17, 26–28]. CrSI monolayer has the highest Curie temperature about 170 K among CrSX [29–31]. While the anisotropic magnetic transport and MTJ performance of the CrSI monolayer are rarely reported, which greatly restricts the development of giant TMR in 2D MTJ research.

Here, we investigated the crystal structure and magnetic property of CrSI monolayer, and found that it is a ferromagnetic semiconductor and the Curie temperature reaches about 180 K. The Li atoms adsorb on the CrSI monolayer (forming Li-CrSI) can gain the electrons of Cr atoms and push the the Fermi level toward the conduction band, thus making the Li-CrSI becomes ferromagnetic half-metallic. The Li-CrSI monolayer show a high Curie temperature of 300 K, which is a perfect MTJs electrode material. Thus we designed a lateral Li-CrSI/CrSI/Li-CrSI monolayer MTJ formed by a ferromagnetic CrSI barrier and two half-metallic Li-CrSI electrodes. The TMR of the MTJs along *b* transport direction is 3 orders of magnitude times larger than that of *a* transport direction, which should result from the different spin filtering ability along the two directions. The TMR of *b* transport direction in MTJ is 7.67×10^{14}, which is significantly higher than that of any reported lateral MTJs based on 2D materials. Our results provide a promising avenue for designing lateral MTJs with giant TMR and high Curie temperature.

2 Methods

The first-principles calculations based on the density functional theory (DFT) were performed to simulate the electronic and magnetic properties of CrSI and Li-CrSI monolayer. The geometry optimizations were carried out via the Vienna *ab initio* simulation package (VASP) [32, 33]. The generalized gradient approximation (GGA) with the Perdew–Burke–Ernzerhof (PBE) realization was adopted for the exchange-correlation function [34], and the projector augmented wave method [35] was used to treat the core electrons. To avoid the interactions between its period image, a vacuum space of 20 Å was used. The cutoff energy was set to be 400 eV, the energy convergence criteria set to 10^{-6} eV for structure optimization. Phonon spectrum is calculated by the PHONOPY code through the density functional perturbation theory approach [36]. The supercell was set to be $2 \times 2 \times 1$ for CrSI and Li-CrSI monolayer, and we employed $9 \times 6 \times 1$ Γ-centered Monkhorst-Pack k-mesh for lattice relax and that of $15 \times 11 \times 1$ for density of states. The electron correlation effect for the localized 3d orbitals of Cr atoms was treated by an effective on-site Hubbard term U of 3 eV [24, 37, 38]. For unit cell of CrSI monolayer, the Heyd–Scuseria–Ernzerhof (HSE06) hybrid functional is used to obtain a more accurate bandgap [39]. The Curie temperatures were estimated by using the Monte Carlo simulations as implemented in the VAMPIRE atomistic simulation package [40]. Quantum transport calculations of Li-CrSI/CrSI/Li-CrSI MTJs were performed using the Nanodcal software package based on DFT combined with the non-equilibrium Green's function [41]. Because *a* and *b* direction atomic structure are different for CrSI monolayer, the Brillouin zone were sampled using $1 \times 100 \times 1$ and $100 \times 1 \times 1$ k-point grid in the transport calculations, respectively. To obtain the magnetic tunneling performance at equilibrium states, the exchange-correlation functional is set to GGA_PBE96 and the spin-resolved conductance is calculated by [42, 43]

$$G_\sigma = \frac{e^2}{h} \sum_{k_{//}} T_\sigma (E_F, k_{//}, V = 0) \quad (1)$$

where e is the electron charge, h is the Planck constant, and T_σ (E_F, $k_{//}$, V) is the spin-resolved transmission coefficient with spin σ ($\sigma = \uparrow, \downarrow$) at the Fermi level E_F and transverse Bloch wave vector $k_{//} = (k_x, k_y)$ under bias V, and $V = 0$ at equilibrium states. The TMR ratio is defined as TMR = $(G_{PC} - G_{APC})/G_{PC}$, where G_{PC} and G_{APC} are the total conductance for the parallel configuration (PC) and antiparallel configuration (APC) of magnetizations of two electrodes, respectively. At zero bias when all currents vanish, we use the transmission coefficient at the Fermi level to calculate TMR.

3 Results and discussion

CrSI monolayer has a distorted orthorhombic lattice belonging to the *Pmmn* space group (Figs. 1(a) and 1(b)). The optimized lattice constants of CrSI monolayer are calculated to be a = 3.76 Å, b = 4.81 Å, respectively, which is consistent with previous work [24, 29–31, 37]. The detailed lattice parameters and values of the fully optimized CrSI monolayer are presented in Fig. S1 and Table S1 in the Electronic Supplementary Material (ESM). To confirm the stability of the crystal structure, the phonon spectrum is calculated using PHONOPY software. The phonon spectra of CrSI monolayer demonstrated that there is no imaginary frequency throughout the Brillouin zone (Fig. S2 in the ESM), indicating CrSI monolayer is dynamically stable.

DFT were performed to calculate the magnetic ground states (MGS) of CrSI monolayer. The energies of ferromagnetic (FM) configurations and four antiferromagnetic (AFM) configurations with $2 \times 2 \times 1$ supercell (Fig. 1(c)) are calculated and the results show that the CrSI monolayer prefers the FM ground state (Table S2 in the ESM). Meanwhile, the magnetic moment of Cr atoms is 3.32 μ_B, and the induced magnetic moments of S atoms and I atoms are −0.23 and −0.1 μ_B in the FM ground state, respectively.

The magnetic anisotropy energy (MAE) with the consideration of SOC of the CrSI monolayer is further studied. The MAE is defined as: $E_{MAE} = E_{in} - E_{out}$, where E_{in}, E_{out} are the total energy of in-plane and out-of-plane, respectively. It is found that the easy magnetic axis is in the plane with a very small value of −0.06 meV. The band structures calculated by the HSE06 functional show that CrSI monolayer is an indirect band gap semiconductor, with a band gap energy of 1.14 eV in spin-up (black line) and a band gap energy of 3.32 eV in spin-down (red line) (Fig. 1(d)), which is consistent with the previous theoretical result [24, 31, 37]. The density of states (DOS) study show that the conduction band is mainly contributed by Cr atoms, while the valence band is contributed by Cr, S and I atoms near the Fermi level (Fig. S3 in the ESM).

The Cuire temperature (T_C) of the CrSI monolayer is estimated by using the Monte Carlo simulations based on an effective classical spin model [24, 40, 44]

$$\boldsymbol{H} = -\frac{1}{2} \sum_{i,j} J_{ij} \boldsymbol{S}_i \cdot \boldsymbol{S}_j - K \sum_i \left(\boldsymbol{S}_i^Z\right)^2 \quad (2)$$

where J_{ij} is the exchange coupling constant between Cr atoms i and

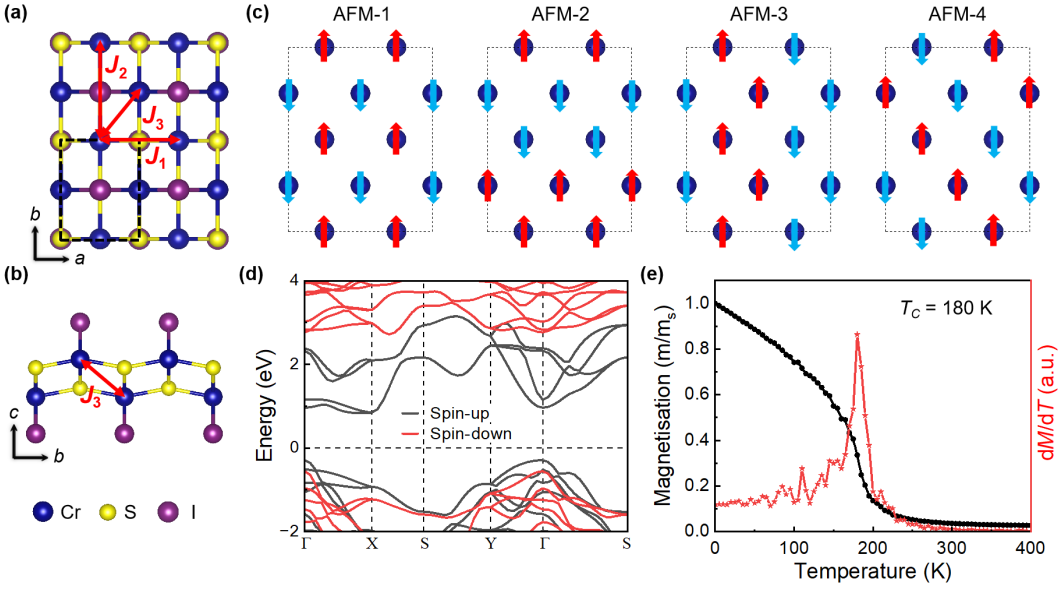

Figure 1 Crystal structure and band structure of CrSI monolayer. (a) Top view and (b) side view of CrSI monolayer crystal structure. The unit cell is marked by a black dotted line, and the red double arrow lines indicate the exchange coupling model. J_1, J_2, J_3 represents the exchange coupling of two neighboring Cr atoms, respectively. (c) The four antiferromagnetic configurations of 2 × 2 × 1 supercell as AFM-1, AFM-2, AFM-3 and AFM-4, respectively. Red arrows indicate the spin-up direction, and blue arrows indicate the spin-down direction of Cr atoms. (d) Band structure calculated by the HSE06 functional of CrSI unit cell. The Fermi energy is set to zero. (e) Variation of the staggered magnetization with respect to the temperature for CrSI monolayer.

j, and $\boldsymbol{S}_i$ is the normalized spin vector on the Cr site i, K is the magnetic anisotropy strength. For simplicity, only the nearest-, second nearest-, and third nearest-neighbor exchanges constant J_1, J_2 and J_3 is considered (Fig. 1(a)). The exchange coupling constants are calculated by using the energy mapping method (Table S3 in the ESM). The T_C is determined from the variation of mean sublattice magnetization with respect to the temperature (Fig. 1(e)), the estimated T_C is about 180 K, which is consistent with the previous theoretical work [25, 29, 30].

Further, the electromagnetic properties of one Li atom adsorbed in a 2 × 2 × 1 supercell of the CrSI monolayer (Li-CrSI) is investigated (Fig. 2(a)). The Li atom is in the middle of the 2 × 2 × 1 supercell and surrounded by four I atoms (Fig. 2(a)). Here, the concentration of Li atom adsorption is 25%. The structural stability of Li-CrSI is studied by calculating the adsorption energies. The adsorption energy (ΔE_{ads}) is defined as

$$\Delta E_{ads} = E_{CrSI} + E_{Li} - E_{Li\text{-}CrSI} \quad (3)$$

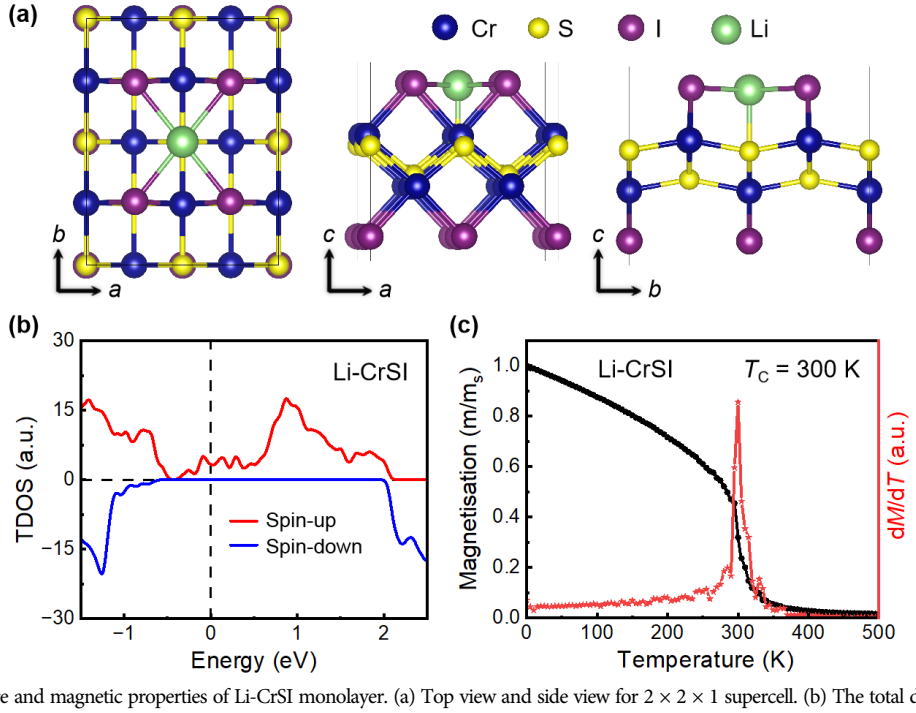

Figure 2 Atomic structure and magnetic properties of Li-CrSI monolayer. (a) Top view and side view for 2 × 2 × 1 supercell. (b) The total density of states and (c) the Curie temperature of Li-CrSI monolayer.

where E_{CrSI} is the total energies of CrSI monolayer, E_{Li} is the energy of isolated Li atom, and $E_{Li\text{-}CrSI}$ is the energy of Li adsorbed CrSI monolayer. The calculated ΔE_{ads} is 3.76 eV (Table S4 in the ESM), demonstrating that the Li atom can be stably adsorbed on the CrSI monolayer.

The total DOS (TDOS) show that the CrSI monolayer transforms from a FM semiconductor to a FM half-metallic after Li atoms adsorbed (Fig. 2(b)). The atomic projected density of states (PDOS) demonstrate that Cr atoms occupy a dominant position at the Fermi level (Fig. S4(a) in the ESM), which means that the Cr atoms gain electrons and pushing the Fermi level toward the conduction band. Differential charge density (DCD) distribution can be used to distinguish characteristics of charge distribution and transfer of the material. The DCD ($\Delta\rho$) is given by

$$\Delta\rho = \rho_{Li\text{-}CrSI} - \rho_{CrSI} - \rho_{Li} \quad (4)$$

where $\rho_{Li\text{-}CrSI}$, ρ_{CrSI} and ρ_{Li} are the charge densities of the Li-CrSI system, CrSI monolayer, and isolated Li atom, respectively. The top view (Fig. S4(b) in the ESM) and side view (Fig. S4(c) in the ESM) of DCD clearly depicts that charge is accumulated on the Cr atoms, as well as in the region between the substrate and adatom. The T_C of the Li-CrSI monolayer is estimated be 300 K using the Monte Carlo simulations (Fig. 2(c)). This means that Li atomic adsorption not only results in half-metallicity but also increases the T_C of the CrSI monolayer.

The CrSI monolayer is a magnetic semiconductor, while Li-CrSI monolayer is a nearly 100% spin-polarized half-metal, so we design a lateral MTJ composed of the Li-CrSI/CrSI/Li-CrSI monolayer, in which the CrSI barrier and the half-metallic Li-CrSI electrode are seamlessly joint together by covalent bonds at the interfaces. Because the atomic structure of CrSI monolayer along *a* and *b* direction are different, two MTJs with different transport directions are further investigated. One is to set the transport direction along the *a* direction (Fig. 3(a)), and the other is to set the transport direction along the *b* direction (Fig. 3(b)). Based on the 2 × 2 × 1 supercell unit, the left and right electrodes contain two supercell units, and the central scattering region contains six supercell unit along the transport direction.

To tune the transport properties, the magnetic configuration of monolayer Li-CrSI electrodes is set as PC or APC. We calculated the spin-resolved conductance of PC ($G_{PC\text{-}up}$ for spin-up, $G_{PC\text{-}dw}$ for spin-down, $G_{PC} = G_{PC\text{-}up} + G_{PC\text{-}dw}$) and APC ($G_{APC\text{-}up}$ for spin-up, $G_{APC\text{-}dw}$ for spin-down, $G_{APC} = G_{APC\text{-}up} + G_{APC\text{-}dw}$), and obtained the TMR ratios for two MTJs (Table 1). In the PC, since the half-metallic carriers of the left and right electrodes are both spin-up electrons, spin-up current can flow through the device. Therefore, the $G_{PC\text{-}up}$ with a value of 0.13 e^2/h for *a* transport direction and 0.79 e^2/h for *b* transport direction is considerable in both transmission directions. While there is no electron in spin-down near Fermi level, so the $G_{PC\text{-}dw}$ are zero. In the APC, by reversing the direction of the electric field of the right electrode, the left electrode has spin-up electrons while the right electrode has spin down electrons near the Fermi level. Due to the spin mismatch, both spin channels will be blocked. As a result, the total conductance of PC is much larger than that of APC, producing an ultrahigh TMR of up to 1.06×10^{11} and 7.67×10^{14} in Li-CrSI/CrSI/Li-CrSI MTJs along *a* and *b* transport direction, respectively (Table 1).

Table 1 Spin-resolved conductance *G* (e^2/h) and TMR (%) of lateral MTJs with the transport direction *a* and *b*

	$G_{PC\text{-}up}$	$G_{PC\text{-}dw}$	$G_{APC\text{-}up}$	$G_{APC\text{-}dw}$	TMR (%)
a	0.13	0.0	8.10×10^{-13}	4.20×10^{-13}	1.06×10^{11}
b	0.79	0.0	4.93×10^{-16}	1.50×10^{-17}	7.67×10^{14}

Meanwhile, the spin-resolved local density of states (LDOS) of Li-CrSI/CrSI/Li-CrSI MTJs along *a* and *b* transport direction indicate that there are states connecting the left and right half-metallic Li-CrSI electrodes at the Fermi level in the spin-up channel (Fig. S5(a) in the ESM and Fig. 4(a)), enabling spin-up electrons to transport through the barrier of CrSI. While there are no states in both electrode regions in the spin-down channel (Figs. S5(b)–S5(d) in the ESM and Figs. 4(b)–4(d)), which blocks the spin-down tunnel through the MTJs. So, the giant TMR of the MTJs is mainly resulted from the half-metallic property of Li-CrSI, which allows only spin-up electrons to go through the barrier while blocks the spin-down electrons.

The above result showed that the TMR along *b* transport direction (10^{14}) is about 3 orders of magnitude larger than that of *a* transport direction (10^{11}). The difference of the TMR should result from the different spin filtering ability of the CrSI channel along two directions. According to the WBK approximation, the tunnel current density (*D*) of the MTJ can be described by [45]

$$D = \frac{e}{2\pi h(\beta\Delta s)^2}\varphi \exp\left[-\left(\frac{4\pi\beta\Delta s\sqrt{2m}}{h}\right)\sqrt{\varphi}\right] \quad (5)$$

where *e* is the charge of electron, *h* is the Planck's constant, β is the correction factor, Δs is the barrier width, *m* is the mass of electron

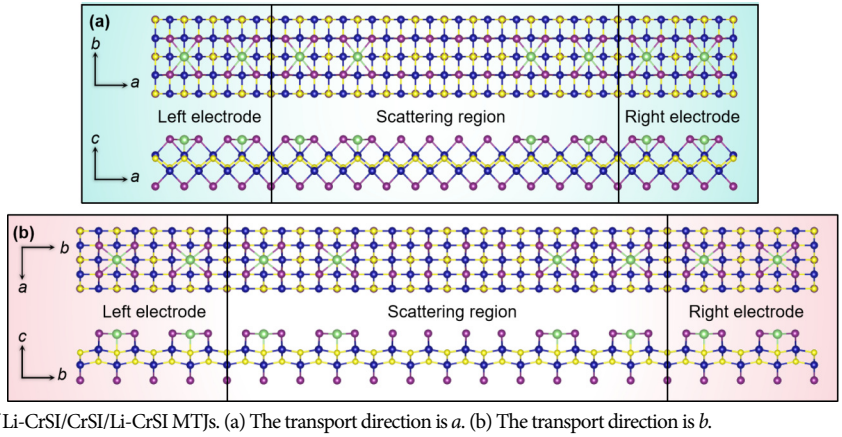

Figure 3 Structure diagram of Li-CrSI/CrSI/Li-CrSI MTJs. (a) The transport direction is *a*. (b) The transport direction is *b*.

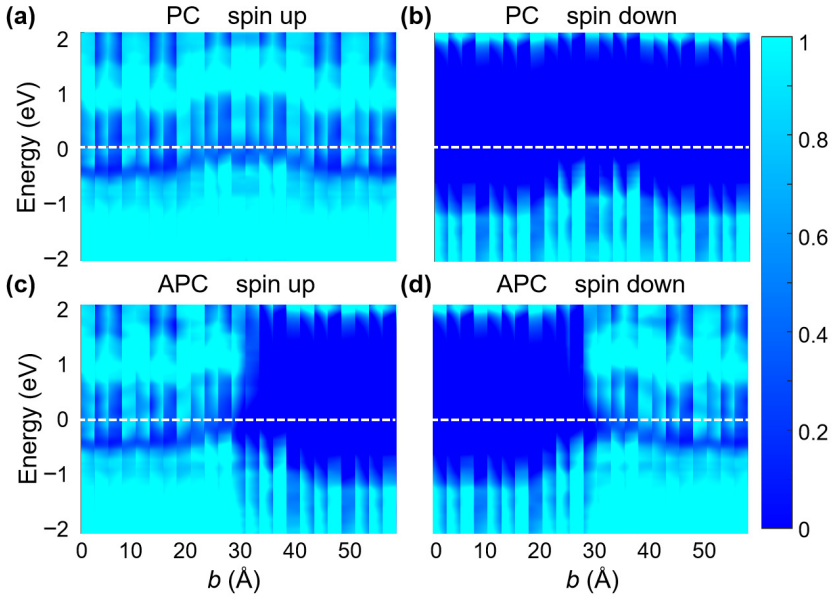

Figure 4 LDOS in the real space along the *b* transport direction of the Li-CrSI/CrSI/Li-CrSI MTJ. (a) Spin-up LDOS and (b) spin-down LDOS under the PC. (c) Spin-up LDOS and (d) spin-down LDOS under the APC.

and φ is the barrier height. Δs of the lateral MTJs along *a* and *b* transport direction are 15 and 19.2 Å, respectively (Fig. 3). For one transport direction, the difference in tunnel current density between spin-up and spin-down electrons is due to their different φ (the value of conduction band minimum of the CrSI monolayer barrier).

Figure S6 in the ESM shows the schematic diagram of first Brillouin zone for CrSI monolayer, which is taken the symmetric point X in the *b* direction and the symmetric point Y in the *a* direction. We extracted φ of the spin up and spin down from the band structure (Fig. 1(d)) along *a* and *b* transport direction, and plotted the schematic of rectangular potential barrier of the lateral MTJs (Figs. 5(a) and 5(b)). Compared with the *a* transport direction, spin-up electrons are more likely to tunnel through the barrier and spin-down electrons are less likely to tunnel through the barrier along the *b* transport direction. Thus the spin filtering ability of the CrSI monolayer barrier of the MTJ between *a* and *b* transport direction is huge, leading to the different TMR.

We compared the TMR of recent work on lateral MTJs based on 2D magnetic materials with our work (Fig. 5(b)), and found that the TMR of the Li-CrSI/CrSI/Li-CrSI MTJs is very high in either the *a* transport direction or the *b* transport direction. Our TMR of the MTJ along *b* transport direction is 7.67×10^{14}, which is significantly higher than that of any reported 2D lateral MTJs. These results suggest that the Li-CrSI/CrSI/Li-CrSI MTJs is a promising spintronic device with a giant TMR and perfect spin filtering ability.

4 Conclusions

We have investigated the crystal structure and magnetic property of CrSI monolayer, and found that it is a ferromagnetic semiconductor with a Curie temperature of about 180 K. The Li-CrSI is ferromagnetic half-metallic with a high Curie temperature of 300 K. Further we designed a lateral Li-CrSI/CrSI/Li-CrSI monolayer MTJ formed by a ferromagnetic CrSI barrier and two

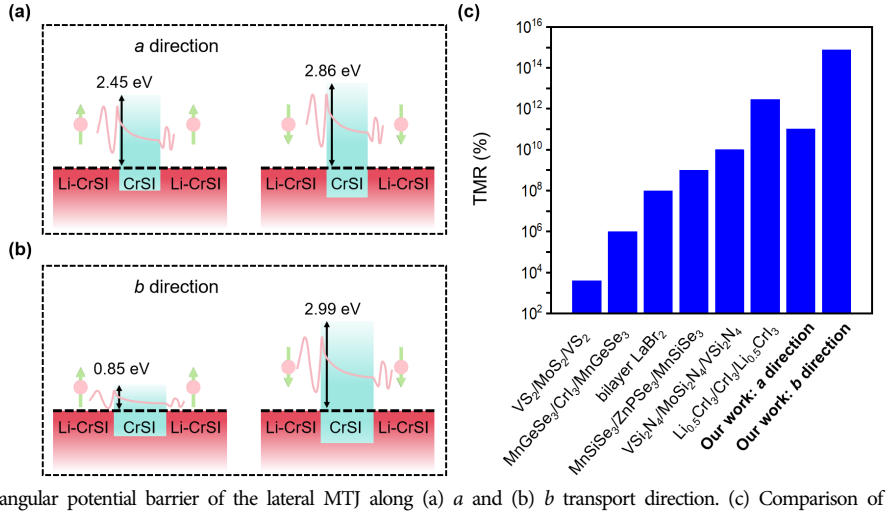

Figure 5 Schematic of rectangular potential barrier of the lateral MTJ along (a) *a* and (b) *b* transport direction. (c) Comparison of TMR for 2D lateral MTJs ($VS_2/MoS_2/VS_2$ [46], $MnGeSe_3/CrI_3/MnGeSe_3$ [47], bilayer $LaBr_2$ [43], $MnSiSe_3/ZnPSe_3/MnSiSe_3$ [48], $VSi_2N_4/MoSi_2N_4/VSi_2N_4$ [49], $Li_{0.5}CrI_3/CrI_3/Li_{0.5}CrI_3$ [21], and our work).

half-metallic Li-CrSI electrodes. The TMR of the MTJs along the *b* transport direction is 3 orders of magnitude times larger than that of the *a* transport direction, which should result from the different spin filtering ability of the CrSI monolayer barrier along the two direction. The TMR of the MTJ along *b* transport direction is 7.67×10^{14}, which is significantly higher than that of any reported 2D lateral MTJs. Our results demonstrate that lateral Li-CrSI/CrSI/Li-CrSI heterosturcture has the huge potential in the application of MTJs with giant TMR, which is expected to promote the development of high-performance spintronics devices.

Electronic Supplementary Material: Supplementary material (calculate exchange coupling constants method, structural parameters, phonon spectra, ferromagnetic and antiferromagnetic energies, projected density of states, exchange coupling constant values of CrSI monolayer; adsorption energy and PDOS of Li-CrSI monolayer; LDOS of the Li-CrSI/CrSI/Li-CrSI MTJ along the *a* transport direction; first Brillouin zone for CrSI monolayer) is available in the online version of this article at https://doi.org/10.26599/NR.2025.94907188.

Data availability

All data needed to support the conclusions in the paper are presented in the manuscript and the Electronic Supplementary Material. Additional data related to this paper may be requested from the corresponding author upon request.

Acknowledgements

This work was supported by the National Natural Science Foundation of China (Nos. 62322406, 62174051, and 62122084), the National Key Research and Development Program of the Ministry of Science and Technology (Nos. 2024YFA1208401 and 2022YFB4400100), the Natural Science Foundation of Hunan Province (No. 2024JJ6115), the Shenzhen Basic Research Project (No. JCYJ20210324142012035), and Natural Science Foundation of Chongqing, China (No. cstc2021jcyj-msxmX0126). We gratefully acknowledge HZWTECH for providing computation facilities.

Declaration of competing interest

All the contributing authors report no conflict of interests in this work.

Author contributions

Q.-Q. L.: Data curation, project administration, validation, writing manuscript. Z.-F. D.: Data curation, validation. W.-W. L.: Data curation, validation. R. Y.: Project administration, validation, writing manuscript. B. L.: Project administration, validation, writing manuscript. K.-Q. C.: Project administration, validation, writing manuscript.

Use of AI statement

None.

References

[1] Moodera, J. S.; Kinder, L. R.; Wong, T. M.; Meservey, R. Large magnetoresistance at room temperature in ferromagnetic thin film tunnel junctions. *Phys. Rev. Lett.* **1995**, *74*, 3273–3276.

[2] Zhu, W. K.; Zhu, Y. M.; Zhou, T.; Zhang, X. P.; Lin, H. L.; Cui, Q. R.; Yan, F. G.; Wang, Z. A.; Deng, Y. C.; Yang, H. X. et al. Large and tunable magnetoresistance in van der Waals ferromagnet/semiconductor junctions. *Nat. Commun.* **2023**, *14*, 5371.

[3] Zhu, Y.; Chi, B. Y.; Jiang, L. N.; Guo, X. Y.; Yan, Y.; Han, X. F. Large tunneling electroresistance, tunneling magnetoresistance, and regulatable negative differential conductance in a van der Waals antiferroelectric multiferroic tunnel junction. *Phys. Rev. Appl.* **2023**, *20*, 034010.

[4] Kajale, S. N.; Hanna, J.; Jang, K.; Sarkar, D. Two-dimensional magnetic materials for spintronic applications. *Nano Res.* **2024**, *17*, 743–762.

[5] Liu, H. X.; Honda, Y.; Taira, T.; Matsuda, K. I.; Arita, M.; Uemura, T.; Yamamoto, M. Giant tunneling magnetoresistance in epitaxial $Co_2MnSi/MgO/Co_2MnSi$ magnetic tunnel junctions by half-metallicity of Co_2MnSi and coherent tunneling. *Appl. Phys. Lett.* **2012**, *101*, 132418.

[6] Ikeda, S.; Hayakawa, J.; Ashizawa, Y.; Lee, Y. M.; Miura, K.; Hasegawa, H.; Tsunoda, M.; Matsukura, F.; Ohno, H. Tunnel magnetoresistance of 604% at 300 K by suppression of Ta diffusion in CoFeB/MgO/CoFeB pseudo-spin-valves annealed at high temperature. *Appl. Phys. Lett.* **2008**, *93*, 082508.

[7] Li, Q. Q.; Li, S.; Wu, D.; Ding, Z. K.; Cao, X. H.; Huang, L.; Pan, H.; Li, B.; Chen, K. Q.; Duan, X. D. Magnetic properties manipulation of $CrTe_2$ bilayer through strain and self-intercalation. *Appl. Phys. Lett.* **2021**, *119*, 162402.

[8] Cui, Q. R.; Liang, J. H.; Shao, Z. J.; Cui, P.; Yang, H. X. Strain-tunable ferromagnetism and chiral spin textures in two-dimensional Janus chromium dichalcogenides. *Phys. Rev. B* **2020**, *102*, 094425.

[9] He, R.; Wang, D.; Luo, N. N.; Zeng, J.; Chen, K. Q.; Tang, L. M. Nonrelativistic spin-momentum coupling in antiferromagnetic twisted bilayers. *Phys. Rev. Lett.* **2023**, *130*, 046401.

[10] Zhang, T. L.; Du, J. T.; Wang, W. J.; Wu, K. M.; Yue, S.; Liu, X. F.; Shen, W. F.; Hu, C. G.; Wu, M. H.; Qu, Z. et al. Strong in-plane optical anisotropy in 2D van der Waals antiferromagnet VOCl. *Nano Res.* **2023**, *16*, 7481–7488.

[11] Li, B.; Wan, Z.; Wang, C.; Chen, P.; Huang, B.; Cheng, X.; Qian, Q.; Li, J.; Zhang, Z. W.; Sun, G. Z. et al. Van der Waals epitaxial growth of air-stable $CrSe_2$ nanosheets with thickness-tunable magnetic order. *Nat. Mater.* **2021**, *20*, 818–825.

[12] Ng, J. Q.; Wu, Q. Y.; Ang, Y. S.; Ang, L. K. Electric field and strain tunable band gap and band alignments of $MoSi_2N_4$/MSe (M = In, Ga) van der Waals heterostructures. *RSC Appl. Interfaces* **2024**, *1*, 1156–1165.

[13] Guo, X. Y.; Zhang, X. L.; Zhu, Y.; Liu, Y. H.; Han, X. F.; Yan, Y. Effective control of magnetism and transport properties of monolayer WV_2N_4 with two magnetic atomic layers and its van der Waals heterostructure. *Appl. Phys. Lett.* **2024**, *125*, 112402.

[14] Wang, C.; Zhou, X. Y.; Zhou, L. W.; Pan, Y. H.; Lu, Z. Y.; Wan, X. G.; Wang, X. Q.; Ji, W. Bethe-slater-curve-like behavior and interlayer spin-exchange coupling mechanisms in two-dimensional magnetic bilayers. *Phys. Rev. B* **2020**, *102*, 020402.

[15] Li, Q. Q.; Liu, W. W.; Ding, Z. K.; Pan, H.; Cao, X. H.; Xiao, W. H.; Luo, N. N.; Zeng, J.; Tang, L. M.; Li, B. et al. Stacking- and strain-dependent magnetism in Janus CrSTe bilayer. *Appl. Phys. Lett.* **2023**, *122*, 121902.

[16] Song, T. C.; Cai, X. H.; Tu, M. W. Y.; Zhang, X. O.; Huang, B.; Wilson, N. P.; Seyler, K. L.; Zhu, L.; Taniguchi, T.; Watanabe, K. et al. Giant tunneling magnetoresistance in spin-filter van der Waals heterostructures. *Science* **2018**, *360*, 1214–1218.

[17] Chen, Y. L.; Samanta, K.; Shahed, N. A.; Zhang, H. J.; Fang, C.; Ernst, A.; Tsymbal, E. Y.; Parkin, S. S. P. Twist-assisted all-antiferromagnetic tunnel junction in the atomic limit. *Nature* **2024**, *632*, 1045–1051.

[18] Yang, R. J.; Mei, L.; Lin, Z. Y.; Fan, Y. Y.; Lim, J.; Guo, J. H.; Liu, Y. J.; Shin, H. S.; Voiry, D.; Lu, Q. Y. et al. Intercalation in 2D materials and *in situ* studies. *Nat. Rev. Chem.* **2024**, *8*, 410–432.
[19] Ilyas, A.; Wu, H. F.; Usman, T.; Khan, S. A.; Deng, R. R. The induction of half-metallicity and enhanced ferromagnetism in a $Cr_2Ge_2Te_6$ monolayer via electron doping and alkali metal adsorption. *J. Mater. Chem. C* **2021**, *9*, 5952–5960.
[20] Wang, F.; Zhang, Y. L.; Yang, W. J.; Zhang, J. J.; Zhang, H. S.; Xu, X. H. Topological half-metallic features in alkali metal doped $CrCl_3$ monolayers. *Phys. Rev. B* **2023**, *107*, 174405.
[21] Li, F. F.; Yang, B. S.; Zhu, Y.; Han, X. F.; Yan, Y. Ultrahigh tunneling magnetoresistance in van der Waals and lateral magnetic tunnel junctions formed by intrinsic ferromagnets $Li_{0.5}CrI_3$ and CrI_3. *Appl. Phys. Lett.* **2020**, *117*, 022412.
[22] Wang, Z. X.; Zheng, H. F.; Chen, A.; Ma, L.; Hong, S. J.; Rodriguez, E. E.; Woehl, T. J.; Shi, S. F.; Parker, T.; Ren, S. Q. Room-temperature CrI_3 magnets through lithiation. *ACS Nano* **2024**, *18*, 23058–23066.
[23] Xu, Q. F.; Xie, W. Q.; Lu, Z. W.; Zhao, Y. J. Theoretical study of enhanced ferromagnetism and tunable magnetic anisotropy of monolayer CrI_3 by surface adsorption. *Phys. Lett. A* **2020**, *384*, 126754.
[24] Wang, C.; Zhou, X. Y.; Zhou, L. W.; Tong, N. H.; Lu, Z. Y.; Ji, W. A family of high-temperature ferromagnetic monolayers with locked spin-dichroism-mobility anisotropy: MnNX and CrCX (X = Cl, Br, I; C = S, Se, Te). *Sci. Bull.* **2019**, *64*, 293–300.
[25] Han, R. L.; Hou, H. Q.; Yan, Y. Large perpendicular magnetic anisotropy, high curie temperature, and half-metallicity in monolayer CrSI induced by substitution doping. *J. Magn. Magn. Mater.* **2023**, *584*, 171074.
[26] Boix-Constant, C.; Mañas-Valero, S.; Ruiz, A. M.; Rybakov, A.; Konieczny, K. A.; Pillet, S.; Baldoví, J. J.; Coronado, E. Probing the spin dimensionality in single-layer CrSBr Van Der Waals heterostructures by magneto-transport measurements. *Adv. Mater.* **2022**, *34*, 2204940.
[27] Liu, H. Y.; Yang, H.; Zheng, Y. J. Strong magnetic anisotropy and magnetoelastic coupling in chromium chalcohalide monolayers. *Phys. Rev. B* **2024**, *109*, 064425.
[28] Xu, B.; Li, S. C.; Jiang, K.; Yin, J.; Liu, Z. G.; Cheng, Y. C.; Zhong, W. Y. Switching of the magnetic anisotropy via strain in two dimensional multiferroic materials: CrSX (X = Cl, Br, I). *Appl. Phys. Lett.* **2020**, *116*, 052403.
[29] Guo, Y. L.; Zhang, Y. H.; Yuan, S. J.; Wang, B.; Wang, J. L. Chromium sulfide halide monolayers: Intrinsic ferromagnetic semiconductors with large spin polarization and high carrier mobility. *Nanoscale* **2018**, *10*, 18036–18042.
[30] Han, R. L.; Hou, H. Q.; Xue, X. M.; Yan, Y. Enhancement of perpendicular magnetic anisotropy and curie temperature in V-doped two-dimensional CrSI Janus semiconductor monolayer. *J. Phys. Chem. C* **2023**, *127*, 2003–2011.
[31] Han, R. L.; Xue, X. M.; Yan, Y. Hole-doping-induced perpendicular magnetic anisotropy and high curie temperature in a CrSX (X = Cl, Br, I) semiconductor monolayer. *Nanomaterials* **2023**, *13*, 3105.
[32] Kresse, G.; Hafner, J. *Ab initio* molecular dynamics for liquid metals. *Phys. Rev. B* **1993**, *47*, 558–561.
[33] Kresse, G.; Furthmüller, J. Efficiency of *ab-initio* total energy calculations for metals and semiconductors using a plane-wave basis set. *Comp. Mater. Sci.* **1996**, *6*, 15–50.
[34] Perdew, J. P.; Burke, K.; Ernzerhof, M. Generalized gradient approximation made simple. *Phys. Rev. Lett.* **1996**, *77*, 3865–3868.
[35] Kresse, G.; Joubert, D. From ultrasoft pseudopotentials to the projector augmented-wave method. *Phys. Rev. B* **1999**, *59*, 1758–1775.
[36] Mann, S.; Rani, P.; Kumar, R.; Jindal, V. K. DFT study of phonon dispersion in pure graphene. *AIP Conf. Proc.* **2015**, *1675*, 030035.
[37] Xuan, X. W.; Yang, Z. Y.; Du, R.; Zhao, Y. M.; Yan, Y. L.; Liu, C.; Li, H.; Zhang, G. B. Ultralow thermal conductivity and anharmonic rattling in two-dimensional CrSX (X = Cl, Br, I) monolayers. *Mater. Adv.* **2023**, *4*, 4852–4859.
[38] Wang, Y. W.; Luo, N. N.; Zeng, J.; Tang, L. M.; Chen, K. Q. Magnetic anisotropy and electric field induced magnetic phase transition in the van der Waals antiferromagnet CrSBr. *Phys. Rev. B* **2023**, *108*, 054401.
[39] Heyd, J.; Scuseria, G. E.; Ernzerhof, M. Hybrid functionals based on a screened Coulomb potential. *J. Chem. Phys.* **2003**, *118*, 8207–8215.
[40] Evans, R. F. L.; Fan, W. J.; Chureemart, P.; Ostler, T. A.; Ellis, M. O. A.; Chantrell, R. W. Atomistic spin model simulations of magnetic nanomaterials. *J. Phys.: Condens. Matter* **2014**, *26*, 103202.
[41] Taylor, J.; Guo, H.; Wang, J. *Ab initio* modeling of quantum transport properties of molecular electronic devices. *Phys. Rev. B* **2001**, *63*, 245407.
[42] Guo, X. Y.; Yang, B. S.; Zhang, X. L.; Zhu, Y.; Han, X. F.; Yan, Y. Giant tunneling magnetoresistance induced by bias voltage in spin-filter van der Waals magnetic tunnel junctions with an interlayer antiferromagnetic semiconductor barrier. *Phys. Rev. B* **2021**, *104*, 144423.
[43] Chen, Q. Q.; Zheng, X. H.; Jiang, P.; Zhou, Y. H.; Zhang, L.; Zeng, Z. Electric field induced tunable half-metallicity in an *A*-type antiferromagnetic bilayer $LaBr_2$. *Phys. Rev. B* **2022**, *106*, 245423.
[44] Asselin, P.; Evans, R. F. L.; Barker, J.; Chantrell, R. W.; Yanes, R.; Chubykalo-Fesenko, O.; Hinzke, D.; Nowak, U. Constrained Monte Carlo method and calculation of the temperature dependence of magnetic anisotropy. *Phys. Rev. B* **2010**, *82*, 054415.
[45] Simmons, J. G. Generalized formula for the electric tunnel effect between similar electrodes separated by a thin insulating film. *J. Appl. Phys.* **1963**, *34*, 1793–1803.
[46] Zhao, P.; Li, J. W.; Jin, H.; Yu, L.; Huang, B. B.; Ying, D. Designing lateral spintronic devices with giant tunnel magnetoresistance and perfect spin injection efficiency based on transition metal dichalcogenides. *Phys. Chem. Chem. Phys.* **2018**, *20*, 10286–10291.
[47] Song, Y. X.; Chai, C. C.; Fan, Q. Y.; Zhang, W.; Yang, Y. T. Lateral magnetic tunnel junctions with a heterointerface-induced half-metallic electrode. *J. Phys. Chem. Solids* **2022**, *167*, 110754.
[48] Tan, J. N.; Yang, G. W.; Ouyang, G. Large tunneling magnetoresistance and its high bias stability in Weyl half-semimetal based lateral magnetic tunnel junctions. *New J. Phys.* **2024**, *26*, 033047.
[49] Wu, Q. Y.; Ang, L. K. Giant tunneling magnetoresistance in atomically thin $VSi_2N_4/MoSi_2N_4/VSi_2N_4$ magnetic tunnel junction. *Appl. Phys. Lett.* **2022**, *120*, 022401.